AUTHOR(S):

Nagakura, Hiroki; Iwakami, Wakana; Furusawa, Shun; Okawa, Hirotada; Harada, Akira; Sumiyoshi, Kohsuke; Yamada, Shoichi; Matsufuru, Hideo; Imakura, Akira

https://doi.org/10.3847/1538-4357/aaac29

CrossMark

Simulations of Core-collapse Supernovae in Spatial Axisymmetry with Full Boltzmann Neutrino Transport

Hiroki Nagakura[1], Wakana Iwakami[2,3] , Shun Furusawa[4], Hirotada Okawa[2,3], Akira Harada[5], Kohsuke Sumiyoshi[6] ,
Shoichi Yamada[3,7] , Hideo Matsufuru[8], and Akira Imakura[9]

[1] TAPIR, Walter Burke Institute for Theoretical Physics, Mail Code 350-17, California Institute of Technology, Pasadena, CA 91125, USA; hirokin@caltech.edu
[2] Yukawa Institute for Theoretical Physics, Kyoto University, Oiwake-cho, Kitashirakawa, Sakyo-ku, Kyoto, 606-8502, Japan
[3] Advanced Research Institute for Science & Engineering, Waseda University, 3-4-1 Okubo, Shinjuku, Tokyo 169-8555, Japan
[4] Interdisciplinary Theoretical Science (iTHES) Research Group, RIKEN, Wako, Saitama 351-0198, Japan
[5] Department of Physics, University of Tokyo, 7-3-1 Hongo, Bunkyo, Tokyo 113-0033, Japan
[6] Numazu College of Technology, Ooka 3600, Numazu, Shizuoka 410-8501, Japan
[7] Department of Science and Engineering, Waseda University, 3-4-1 Okubo, Shinjuku, Tokyo 169-8555, Japan
[8] High Energy Accelerator Research Organization, 1-1 Oho, Tsukuba, Ibaraki 305-0801, Japan
[9] University of Tsukuba, 1-1-1, Tennodai Tsukuba, Ibaraki 305-8577, Japan

Abstract

We present the first results of our spatially axisymmetric core-collapse supernova simulations with full Boltzmann neutrino transport, which amount to a time-dependent five-dimensional (two in space and three in momentum space) problem. Special relativistic effects are fully taken into account with a two-energy-grid technique. We performed two simulations for a progenitor of $11.2\,M_\odot$, employing different nuclear equations of state (EOSs): Lattimer and Swesty's EOS with the incompressibility of $K = 220\,\mathrm{MeV}$ (LS EOS) and Furusawa's EOS based on the relativistic mean field theory with the TM1 parameter set (FS EOS). In the LS EOS, the shock wave reaches $\sim 700\,\mathrm{km}$ at 300 ms after bounce and is still expanding, whereas in the FS EOS it stalled at $\sim 200\,\mathrm{km}$ and has started to recede by the same time. This seems to be due to more vigorous turbulent motions in the former during the entire postbounce phase, which leads to higher neutrino-heating efficiency in the neutrino-driven convection. We also look into the neutrino distributions in momentum space, which is the advantage of the Boltzmann transport over other approximate methods. We find nonaxisymmetric angular distributions with respect to the local radial direction, which also generate off-diagonal components of the Eddington tensor. We find that the $r\theta$ component reaches $\sim 10\%$ of the dominant rr component and, more importantly, it dictates the evolution of lateral neutrino fluxes, dominating over the $\theta\theta$ component, in the semitransparent region. These data will be useful to further test and possibly improve the prescriptions used in the approximate methods.

Key words: hydrodynamics – neutrinos – supernovae: general

1. Introduction

The theoretical study of the explosion mechanism of core-collapse supernovae (CCSNe) has heavily relied on numerical simulations. This is mainly because nearby CCSNe are rare (van den Bergh & Tammann 1991; Cappellaro et al. 1993; Tammann et al. 1994; Reed 2005; Diehl et al. 2006; Maoz & Badenes 2010; Li et al. 2011), and, in fact, SN1987A is the only one close enough to extract some useful information on what happened deep inside the massive star from, among other things, the detection of neutrinos (Bionta et al. 1987; Hirata et al. 1987). Since the CCSNe are intrinsically multiscale, multiphysics, and multidimensional (multi-D) phenomena, their mechanism can be addressed only with detailed numerical simulations.

Unfortunately, even the most advanced multi-D simulations of CCSNe employed approximations one way or another in their numerical treatment of neutrino transport (Marek & Janka 2009; Müller et al. 2012; Bruenn et al. 2013, 2016; Takiwaki et al. 2014; Dolence et al. 2015; Just et al. 2015; Lentz et al. 2015; Melson et al. 2015; O'Connor & Couch 2015; Burrows et al. 2018; Kuroda et al. 2016; Pan et al. 2016;

Roberts et al. 2016; Skinner et al. 2016; Summa et al. 2016; Andresen et al. 2017). Most of them somehow integrated out the angular degrees of freedom in momentum space or neglected nonradial fluxes in neutrino transport. Ott et al. (2008) is the only exception, in which they conducted time-dependent five-dimensional simulations in spatial axisymmetry. However, they ignored relativistic corrections completely, dropping all fluid-velocity-dependent terms, which are crucial for qualitatively correct descriptions of the angular distribution of neutrinos in momentum space (see, e.g., Buras et al. 2006; Lentz et al. 2012).

The best way to calibrate all of these approximate methods should be to compare them with simulations that solve full Boltzmann equations, retaining the angular degree of freedom, for neutrino transport. Under axisymmetry in space, this is now indeed possible, and we have achieved such simulations with the K computer in Japan, one of the best currently available supercomputers with ~ 10 PFLOPS. The validation of our Boltzmann solver has been conducted in a series of papers: the standard tests in static matter distributions meant for radiation transport codes were done in Sumiyoshi & Yamada (2012); Nagakura et al. (2014) coupled the Boltzmann solver with a hydrodynamics code of their own construction and tested in dynamical settings the capability of the integrated code to treat special relativistic effects; Nagakura et al. (2017), on the other hand, tested a new module implemented to track the motion of

a proto neutron star (PNS) with a moving grid; very recently, Richers et al. (2017) made a detailed comparison with another Boltzmann solver based on the Monte Carlo method using snapshots from our 2D and 1D simulations and calculating steady-state neutrino distribution functions in the static fluid backgrounds. Having established the reliability of our code with these test computations, we now proceed to present the first series of multi-D simulations of CCSNe with the full Boltzmann neutrino transport. In this paper, we also pay attention to the neutrino angular distributions in momentum space, which are what the Boltzmann solver is meant for in the first place. Throughout this paper, Greek and Latin subscripts denote spacetime and spatial components, respectively. We use the metric signature $-+++$. Unless otherwise stated, we work in units with $c = G = 1$, where c is the speed of light and G is the gravitational constant.

2. Methods and Models

We solve numerically the equations of neutrino-radiation hydrodynamics. We apply the so-called discrete-ordinate method to the Boltzmann equations for neutrino transport, taking fully into account special relativistic effects by virtue of a two-energy-grid technique (Nagakura et al. 2014). It has already incorporated general relativistic capabilities as well, a part of which is utilized to track the proper motion of PNSs (Nagakura et al. 2017). The hydrodynamics and self-gravity are still Newtonian: the so-called central scheme of second-order accuracy in both space and time is employed for the former, and the Poisson equation is solved for the latter.

It should be noted that our treatment of neutrino transport is essentially different from other approximate methods such as the M1 scheme that are commonly employed in the currently most elaborate supernova simulations and are based on the truncated moment formalism one way or another. It is combined with the ray-by-ray approximation in some applications (see, e.g., Müller et al. 2012). In the moment formalism, the Boltzmann equation is angle-integrated in momentum space to obtain an infinite number of equations for angular moments, which are then truncated at some order somehow (see Section 4 for more details). Such approximations reduce the computational cost drastically. On the other hand, they inevitably introduce the so-called closure relation among low-order moments, which are the artificial prescriptions to make the truncated equations self-contained. Although the validity of those prescriptions has been assessed for spherically symmetric cases in the literature (Richers et al. 2017), it remains to be demonstrated in multidimensional and, more importantly, dynamical settings. In sharp contrast, our approach does not employ any such artificial prescription in the neutrino transport except for the finite discretization of the Boltzmann equation, which is all but mandatory for this sort of simulation.

We adopt spherical coordinates (r, θ) covering $0 \leqslant r \leqslant 5000$ km and $0° \leqslant \theta \leqslant 180°$ in the meridian section. We deploy $384(r) \times 128(\theta)$ grid points. Momentum space is also discretized nonuniformly with 20 energy mesh points covering $0 \leqslant \varepsilon \leqslant 300$ MeV and $10(\bar{\theta}) \times 6(\bar{\phi})$ angular grid points over the entire solid angle. The polar and azimuthal angles $(\bar{\theta}, \bar{\phi})$ are locally measured from the radial direction. Three neutrino species are distinguished: electron-type neutrinos ν_e, electron-type antineutrinos $\bar{\nu}_e$, and all of the others, collectively denoted by ν_x.

We pick up a nonrotating progenitor model of 11.2 $M_\odot$ from Woosley et al. (2002). We employ two nuclear equations of state (EOSs): Lattimer & Swesty's EOS with the incompressibility of $K = 220$ MeV (Lattimer & Douglas Swesty 1991) and Furusawa's EOS derived from H. Shen's relativistic mean field EOS with the TM1 parameter set (Furusawa et al. 2011, 2013); the former is softer than the latter (see Sumiyoshi et al. 2004). In the following, they are referred to as the LS and FS EOSs, respectively.[10] The choice of EOS is simply based on the fact that most of the previous simulations employed one of these EOSs. We are currently running similar simulations, but with another EOS: Togashi's nuclear EOS based on the variational method with realistic nuclear potentials (Togashi & Takano 2013) extended by Furusawa et al. (2017) to subnuclear densities; it takes into account the full ensemble of heavy nuclei in nuclear statistical equilibrium. The results will be reported elsewhere (H. Nagakura et al. 2018, in preparation). Neutrino–matter interactions are based on those given by Bruenn (1985), but we have implemented the up-to-date electron capture rates for heavy nuclei (Langanke & Martínez-Pinedo 2000; Langanke et al. 2003; Juodagalvis et al. 2010); they are calculated based on the abundance of heavy nuclei obtained in the FS EOS. The same rates are employed in the LS EOS model just for simplicity. Note also that the LS EOS employs a single-nucleus approximation, and the detailed information on the population of various nuclei is unavailable. In the current simulations, we incorporated the nonisoenergetic scatterings on electrons and positrons as well as the bremsstrahlung in nucleon collisions. We refer readers to Nagakura et al. (2014, 2017) and Sumiyoshi & Yamada (2012) for more details of our code.

We start the simulations in spherical symmetry and switch them to axisymmetric computations at $\sim$1 ms after core bounce when a negative entropy gradient starts to develop behind the shock wave. We seed by hand at this point in time perturbations of 0.1% in the radial velocities at $30 \leqslant r \leqslant 50$ km, where convection is expected to occur (see Figure 2). Note that we do not explicitly consider possible turbulent motions that have already existed in the progenitors before collapse. We then expect in nonrotating models that nonradial motions develop initially in the convectively unstable region and then spread in the rest of the postshock flow. Each model is run up to $t = 300$ ms after bounce.

3. Dynamics

As displayed in Figure 1(a), the shock wave produced at the core bounce expands rather gradually with time for the LS EOS, and its maximum radius reaches $\sim$700 km at $t = 300$ ms. For the FS EOS, on the other hand, the shock wave stalls at $r \sim 200$ km at $t \sim 100$ ms and then starts to recede at $t \sim 250$ ms and shrinks back to $r \sim 100$ km by $t \sim 300$ ms. Although the time evolutions of the average shock radii of the two models are quite similar to each other until $\sim$60 ms after bounce and their deviations become remarkable thereafter, some differences have in fact already appeared in the postshock flows by this time.

In the top two panels of Figure 2, we compare the angle-averaged amplitudes of lateral velocity for the two models. The more reddish the color is, the stronger the lateral motions. It is apparent that they become appreciable initially at $t \sim 10$ ms in

---

[10] The maximum gravitational masses at zero temperature and nonrotating neutron stars are 2.02 $M_\odot$ for LS EOS and 2.21 $M_\odot$ for FS EOS, respectively.
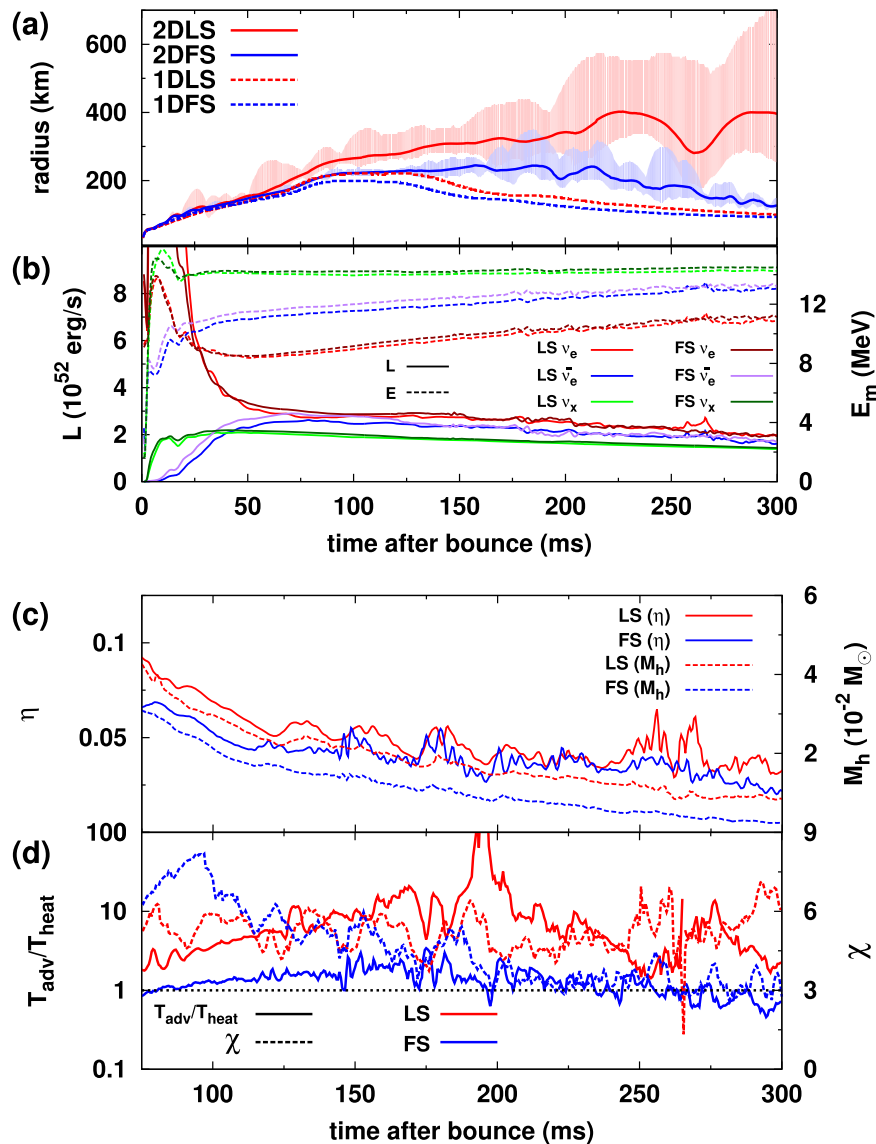
Figure 1. (a) Shock radii as functions of time. The color-shaded regions show the ranges of the shock radii: red for the LS EOS and blue for the FS EOS. The solid lines are the angle-averaged values. For comparison, the corresponding results in spherical symmetry are displayed with dashed lines. (b) Time evolutions of the angle-integrated luminosities (L, solid lines) and the angle-averaged mean energies (E_m, dashed lines) for different species of neutrinos. Both of them are measured at $r = 500$ km. (c) Neutrino-heating efficiency (solid lines) and total mass in the gain region (dashed lines). The heating efficiency is defined as the ratio of the energy deposition rate in the gain region to the sum of the neutrino luminosities of ν_e and $\bar{\nu}_e$. (d) Ratio of the advection to heating timescales (T_{adv}/T_{heat}, with solid lines) and the χ parameter (dashed lines). The dotted black line represents $T_{adv}/T_{heat} = 1$ and $\chi = 3$ for reference.

a region at $r \sim 30$ km almost simultaneously, which marks the onset of the prompt convection. Although the turbulent region extends upward in both models, the amplitudes of the lateral velocity are larger for the LS EOS than for the FS EOS, indicating that the prompt convection is more vigorous in the former. This trend persists until much later times, though, as is also evident from the figure.

The difference in the strength of the prompt convection may be understood from the difference in the Brunt–Väisälä frequencies, which are compared in the lower panels of Figure 2. Reddish colors again imply more rapid (exponential) growth of the convection. As expected, the unstable region emerges at $r \sim 30$–50 km immediately after the switch to the 2D computations for both models. Although this strongly unstable region persists until $t \sim 15$ ms at about the same location for both models, the maximum frequency is larger for

the LS EOS. This difference can be traced back to the difference in photodissociations of heavy nuclei by shock heating. In fact, they are stronger in the LS EOS, and, as a result, the shock is weakened more severely, producing steeper negative entropy gradients in this case. The initial fluctuations produced this way are carried upward by acoustic waves, which are also stronger in the LS EOS. As a consequence, the turbulent motions are more vigorous for the LS EOS than for the FS EOS as already mentioned, a fact that has an important implication for later evolution of the shock waves.

It is interesting that the neutrino luminosities (L) and mean energies (E_m, defined as the ratio of energy density to number density) are almost identical between the two cases (Figure 1(b)). It should be noted, however, that the neutrino-heating efficiency is different, being higher for the LS EOS (see solid lines in Figure 1(c)). This is mainly because the total
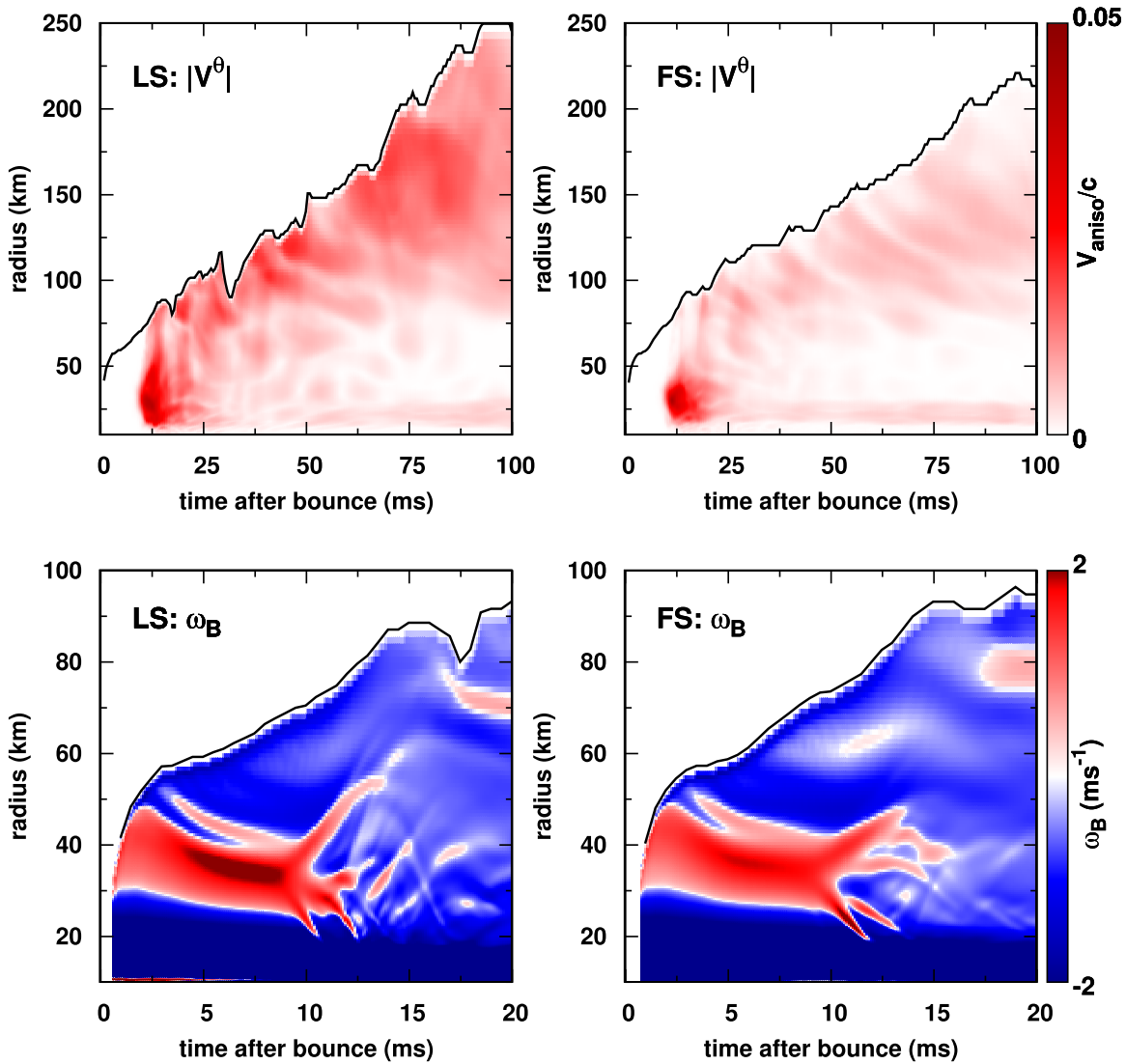
Nagakura et al.

Figure 2. Color contours showing time evolutions of the radial profile of angle-averaged lateral velocities ($|v^\theta|$) until 100 ms after bounce (top) and of Brunt–Väisälä frequencies in the very early postbounce phase up to 20 ms (bottom). Left and right panels present LS and FS EOS models, respectively. The solid line indicates the minimum shock radius in each panel. Note that a positive (negative) sign is assigned to imaginary (real) Brunt–Väisälä frequencies in this figure for convenience.

baryon mass in the gain region, where heating dominates over cooling and the net heating occurs, is consistently larger for the LS EOS than for the FS EOS (dashed lines in the same panel). This in turn seems to be a consequence of the turbulent motions that are more vigorous for the LS EOS, as we mentioned in the previous paragraphs.

Figure 3 compares the entropy and velocity distributions between the two models at $t = 200$ ms. Their postshock morphologies are quite similar to each other, and only the scales are different. In fact, the convection is dominant over the standing accretion shock instability (SASI) in most of the postbounce phase for both models (see the χ parameter (Foglizzo et al. 2006; Iwakami et al. 2014) in Figure 1(d)). In the same panel, we also show the ratio of the advection timescale ($T_{adv} = M_g/\dot{M}$ with M_g and $\dot{M}$ denoting the mass in the gain region and the mass accretion rate, respectively) to the heating timescale ($T_{heat} = |E_{tot}|/\dot{Q}_\nu$ with E_{tot} and $\dot{Q}_\nu$ being the total energy and the heating rate in the gain region, respectively) as solid lines. One can see that it is consistently larger for the LS EOS than for the FS EOS, meaning that the former has more favorable conditions for shock revival than the latter.

The decline of this ratio near the end of the simulation for the LS EOS in spite of a continuous growth of the maximum shock radius is an artifact originating from our choice of the minimum shock radius in the evaluation of the ratio. As displayed in Figure 1(a), the minimum shock radius is still decreasing with time at the end of the simulation. Then the volume of the gain region is underestimated, and, as a result, T_{heat} is overestimated. The fact that the ratio occasionally exceeds unity but still yields no shock revival for the FS EOS indicates that the criterion is not a rigorous condition, which is understood also from the uncertainty in its definition just mentioned. We do not intend to discuss the applicability of the diagnostics any further in this paper, but we still think it is useful in judging, albeit roughly, which model is closer to shock revival.

4. ν Distributions in Momentum Space

Next we turn our attention to novel features of the neutrino distributions in momentum space. We find in our calculations a significant nonaxisymmetry with respect to the radial direction in the neutrino angular distributions. It is produced by lateral
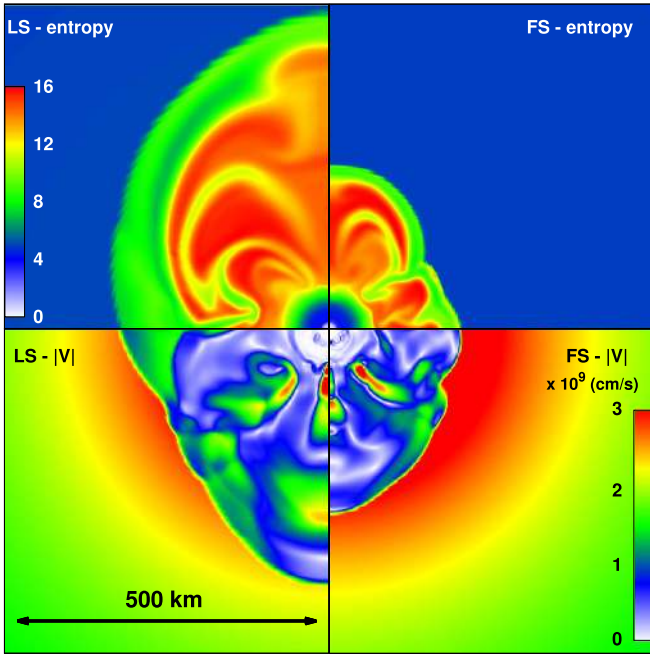
Nagakura et al.

Figure 3. Snapshots of entropy per baryon (upper) and fluid speed (lower) at $t = 200$ ms. Left and right panels are for the LS and FS EOS, respectively.

Figure 4. Angular distributions of ν_e in momentum space at $t_{pb} = 15$ ms for the LS EOS. Different colors correspond to different radial positions (red: $r = 23$ km, green: $r = 39$ km, blue: $r = 49$ km) along the radial ray with the zenith angle of $\theta = 8\pi/15$. The neutrino energy is $\varepsilon = 11.1$ MeV in the fluid rest frame.

inhomogeneities in matter, which are in turn generated by hydrodynamical instabilities. The asymmetry hence appears inevitably in multi-D simulations.

Figure 4 shows as an example the angular distributions of ν_e with an energy of $\varepsilon = 11.1$ MeV at three different radial positions. Each surface displays the neutrino distribution function for different propagation directions normalized by the maximum value in the fluid rest frame. Colors of the surfaces denote the locations on an arbitrarily chosen radial ray. The angular distribution is almost isotropic at $r = 23$ km (red surface), while they become forward-peaked (green and blue surfaces) as the radius increases, a fact that is well known. What is really new here is that they are nonaxisymmetric with respect to the radial direction, which is more apparent in Figure 5, in which the isotropic contributions are subtracted from the original distributions and the resultant ones are renormalized by their maximum values. Note that the feature is robust, occurring irrespective of neutrino energies or species.

It should be mentioned, however, that the nonaxisymmetric angular distributions obtained in the current simulations still have a symmetry with respect to the azimuthal angle ($\bar{\phi}$) in momentum space. This is because these are nonrotating models, and there is a mirror symmetry with respect to the plane spanned by $\bar{e}_r$ and $\bar{e}_\theta$ in momentum space in the absence of rotation. Once rotation is taken into account, the symmetry is lost even in (spatial) axisymmetry. This is why we do not assume this symmetry in our code. In 3D simulations, no symmetry remains in the angular distribution in momentum space. Its characterization is an interesting subject of spatially 3D supernova simulations with multiangle neutrino transport, which are currently being undertaken and will be reported elsewhere later.

The multiangle treatment of neutrino transport in our simulations enables us to evaluate the so-called Eddington tensor (k^{ij}), which characterizes these nonaxisymmetric angular distributions more quantitatively. The Eddington tensor is obtained from the neutrino distribution function (f) as follows.
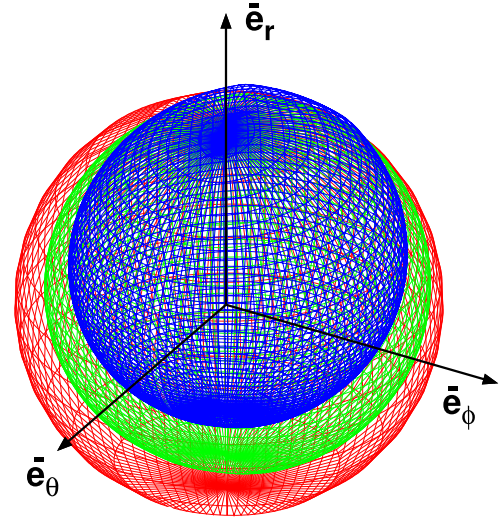
We first define the second angular moment $M^{\mu\nu}$ as

$$M^{\mu\nu}(\varepsilon) \equiv \frac{1}{\varepsilon} \int f(\varepsilon, \Omega_m) p^\mu p^\nu d\Omega_m, \tag{1}$$

where p^μ is the four-momentum of neutrinos, and ε and Ω_m are the corresponding energy and solid angle measured in the fluid rest frame. Then the Eddington tensor k^{ij} is given as

$$k^{ij}(\varepsilon) \equiv \frac{P^{ij}(\varepsilon)}{E(\varepsilon)}, \tag{2}$$

where P^{ij} and E are defined from $M^{\mu\nu}$ as

$$P^{ij}(\varepsilon) \equiv \gamma^i_\mu \gamma^j_\nu M^{\mu\nu}(\varepsilon), \tag{3}$$

$$E(\varepsilon) \equiv n_\mu n_\nu M^{\mu\nu}(\varepsilon), \tag{4}$$

with n_μ and $\gamma^i_\mu (= \delta^i_\mu + n^i n_\mu)$ being the unit vector orthogonal to a hypersurface of constant coordinate time and the projection tensor onto this hypersurface, respectively.

We pay particular attention here to one of the off-diagonal components of the Eddington tensor, $k^{r\theta}$, which are zero in spherical symmetry in space; that is, they are a measure of genuine multidimensional transfer. The left panel in Figure 6(a) shows $k^{r\theta}$ for ν_e with the mean energy at each point. As expected, it is almost zero inside the PNS, where matter is opaque enough to make the neutrino distribution isotropic. It becomes nonzero outside the PNS, however, and increases with radius in accord with the appearance of the nonaxisymmetric structures in the neutrino angular distribution (see Figure 4). In fact, the $k^{r\theta}$ corresponds to the mode with $\ell = 2$, $m = 1$ in the spherical harmonics expansion of the distribution function.

The right panel in Figure 6(a) compares $k^{r\theta}$ obtained from our simulation with that which is evaluated according to the M1 prescription: the Eddington tensor in the M1 prescription (k^{ij}_{M1}) is obtained by replacing P^{ij} in Equation (3) with

$$P^{ij}_{M1}(\varepsilon) = \frac{3\zeta(\varepsilon) - 1}{2} P^{ij}_{thin}(\varepsilon) + \frac{3(1 - \zeta(\varepsilon))}{2} P^{ij}_{thick}(\varepsilon), \tag{5}$$
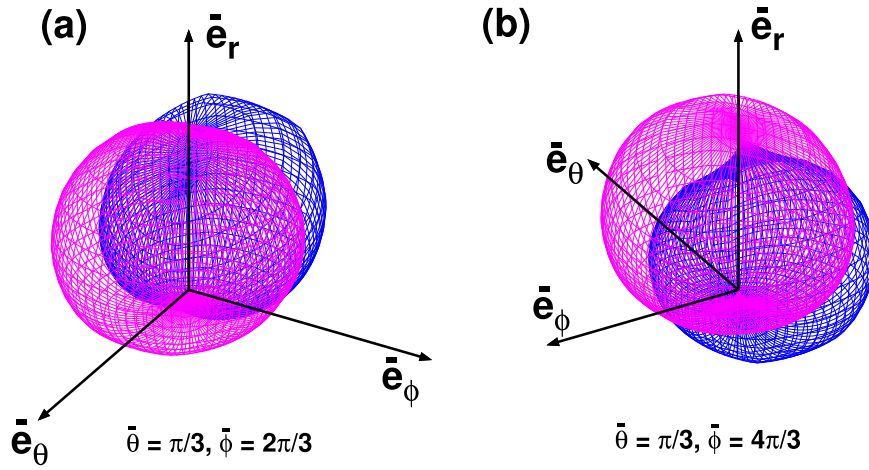
Figure 5. Similar to Figure 4 but with the deviations from spherical symmetry emphasized and viewed from different angles: (a) $\bar{\theta} = \pi/3$ and $\bar{\phi} = 2\pi/3$, (b) $\bar{\theta} = \pi/3$ and $\bar{\phi} = 4\pi/3$. In each panel, the minimum is subtracted isotropically from the original angular distribution, and the resultant distribution is normalized so that the maximum value should always be identical. The blue surface corresponds to the one with the same color in Figure 4, while the purple surface shows another subtracted surface at the same radius but at a different zenith angle, $\theta = 17\pi/45$.

where ζ is referred to as the variable Eddington factor, which we set as

$$\zeta(\varepsilon) = \frac{3 + 4\bar{F}(\varepsilon)^2}{5 + 2\sqrt{4 - 3\bar{F}(\varepsilon)^2}}. \quad (6)$$

In this expression, $\bar{F}$ denotes the so-called flux factor, which is the energy flux normalized with the energy density in the fluid rest frame. The flux factor that we use in this paper is measured in the fluid rest frame (see Shibata et al. 2011 for another option):

$$\bar{F}(\varepsilon) = \left(\frac{h_{\mu\nu} H^\mu(\varepsilon) H^\nu(\varepsilon)}{J(\varepsilon)^2} \right)^{1/2}, \quad (7)$$

where J and H^μ can be expressed in terms of $M^{\mu\nu}$ as

$$J(\varepsilon) = u_\mu u_\nu M^{\mu\nu}(\varepsilon),$$
$$H^\mu(\varepsilon) = -h^\mu_\alpha u_\beta M^{\alpha\beta}(\varepsilon), \quad (8)$$

with u^μ and $h^\mu_\nu (= \delta^\mu_\nu + u^\mu u_\nu)$ being the fluid four-velocity and the projection tensor onto the fluid rest frame, respectively. The optically thick and thin limits of P^{ij} are denoted by P^{ij}_{thick} and P^{ij}_{thin} (Shibata et al. 2011; Just et al. 2015; O'Connor & Couch 2015; Kuroda et al. 2016), which are written as

$$P^{ij}_{\text{thick}}(\varepsilon) = J(\varepsilon) \frac{\gamma^{ij} + 4 V^i V^j}{3} + H^i(\varepsilon) V^j + V^i H^j(\varepsilon),$$
$$P^{ij}_{\text{thin}}(\varepsilon) = E(\varepsilon) \frac{F^i(\varepsilon) F^j(\varepsilon)}{F(\varepsilon)^2}, \quad (9)$$

where V^i denotes the three-dimensional vector of fluid velocity. Here, F^i can be expressed in terms of $M^{\mu\nu}$ as

$$F^i(\varepsilon) = -\gamma^i_\mu n_\nu M^{\mu\nu}(\varepsilon). \quad (10)$$

As clearly seen in this panel, the values of $k^{r\theta}$ are substantially different between the two cases. We find that such discrepancies in $k^{r\theta}$ are rather generic, being insensitive to the choice of the prescription for the Eddington factor (see Just et al. 2015 for various options). They are also systematic in the sense that the increase in the number of grid points in the M1 prescription does not reduce the difference. This is in contrast

to our approach, in which the accuracy is simply improved with the resolution.

Moreover, we find in $k^{r\theta}$ an intriguing correlation/anticorrelation between ν_e and $\bar{\nu}_e$. The two panels of Figure 6(b) compare $k^{r\theta}$ for ν_e and $\bar{\nu}_e$ with the same energy of $\varepsilon = 8.5$ MeV. As can be seen in these panels, they are anticorrelated with each other in the vicinity of PNS ($\lesssim 50$ km), whereas they are positively correlated at larger radii (>80 km). The anticorrelation is particularly remarkable for low-energy neutrinos with $\lesssim 10$ MeV. We find that the sign of $k^{r\theta}$ roughly coincides with that of the lateral neutrino flux, which is shown in Figure 6(c). In fact, it is apparent that the lateral flux is oriented in the opposite directions for ν_e and $\bar{\nu}_e$. This is in turn due to the Fermi degeneracy of ν_e at $r \lesssim 30$ km, which produces opposite trends in the number densities of ν_e and $\bar{\nu}_e$. Since neutrinos flow from high to low ν number density regions in the diffusion regime, the fluxes of ν_e and $\bar{\nu}_e$ should be naturally anticorrelated as a result of the opposite trend in the number densities of ν_e and $\bar{\nu}_e$. We do not know for the moment how this anticorrelation in the fluxes is transferred to that in $k^{r\theta}$. It will be necessary to analyze more in detail the equations of motion for higher moments including $k^{r\theta}$.

Importantly, the anticorrelation is then carried to larger radii by the radial flux and remains nonvanishing even at $r \sim 50$ km, where ν_e is no longer degenerate. On the other hand, at even larger radii, where matter is optically thin to neutrinos, $k^{r\theta}$ is correlated with the local lateral velocity of matter due to relativistic aberration. Note that this positive correlation at large distances is less remarkable than the anticorrelation in the vicinity of PNS (see the equatorial region in Figure 6(b)), since the angular distribution is no longer determined locally and the correlation is somewhat smeared out.

As will be discussed in Section 6, the appropriate treatment of $k^{r\theta}$ is related to the accurate calculation of the neutrino flux, in particular its lateral component (see Equations (11) and (12)). It is true that these correlations/anticorrelations look rather minor, but they may play an important role through the lateral fluxes of neutrinos. In fact, they clearly indicate the intricacy of neutrino transport in nonspherically dynamical settings. It will be interesting to see how well the M1 scheme can reproduce these features and to conceive possible improvements of its prescription.
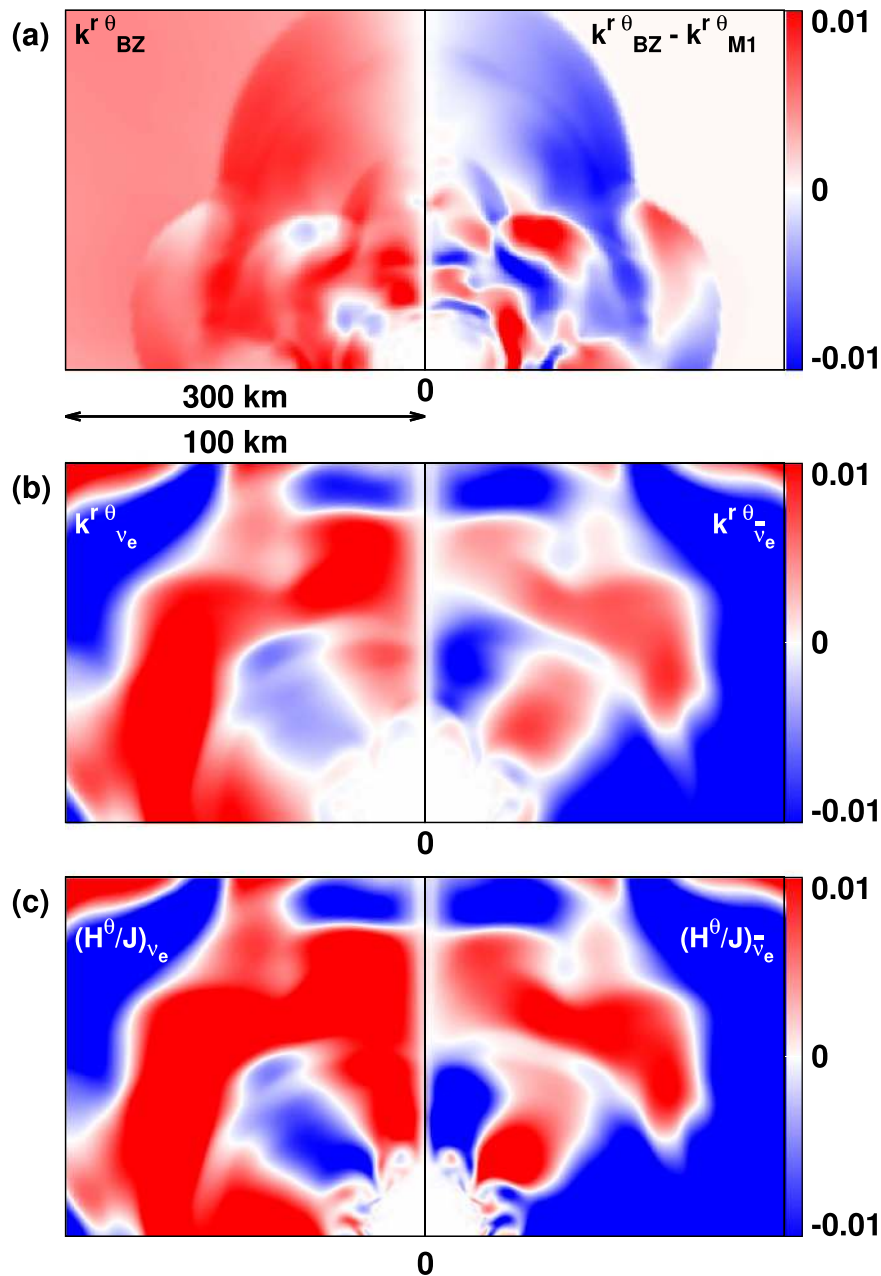
Figure 6. (a) The $(r\theta)$ component of the Eddington tensor $(k^{r\theta})$ for ν_e in the northern hemisphere obtained in our simulation for the FS EOS (left) and its deviation from the M1 prescription (right). The values of $k^{r\theta}$ are evaluated at the mean neutrino energy at each point. (b) $k^{r\theta}$ for ν_e (left) and $\bar{\nu}_e$ (right) on a smaller spatial scale of 100 km. The neutrino energy is fixed to 8.53 MeV in the fluid rest frame. (c) Same as panel (b) but for H^{θ}/J, with H and J being the energy flux and energy densities measured in the fluid rest frame, respectively. The time is $t = 190$ ms in all cases.

5. Angular Resolution in Momentum Space

This study is the first-ever attempt to perform spatially 2D supernova simulations with multiangle and multienergy neutrino transport, taking into account all special relativistic effects completely. It is a legitimate concern, however, that the current simulations may not have a sufficient numerical resolution, especially in momentum space (Richers et al. 2017). In this section, we hence discuss this resolution issue, focusing on the angular resolution in momentum space.

For that purpose, we perform a new high-resolution simulation for the early postbounce phase, whereas for the discussion of the late postbounce phase we employ the results of our previous analyses (Richers et al. 2017) of time-independent solutions of the Boltzmann equations for neutrinos

in given matter distributions; close comparisons were made with the data obtained with Monte Carlo simulations (Richers et al. 2015). Note that although the use of the time-independent solutions for the fixed matter distributions enabled us to conduct rigorous comparisons, its applicability may be limited to the late postbounce phase, where the timescale of variations in the background is indeed long. For the earlier phase, however, we need to consider time-dependent solutions. We hence run a higher-resolution simulation, in which the time evolutions of both neutrino and matter distributions are computed for only 15 ms from the bounce with the LS EOS. We compare the results so obtained with the original ones to see to what extent the angular resolution could affect the outcome. Note, however, that the comparisons are not so
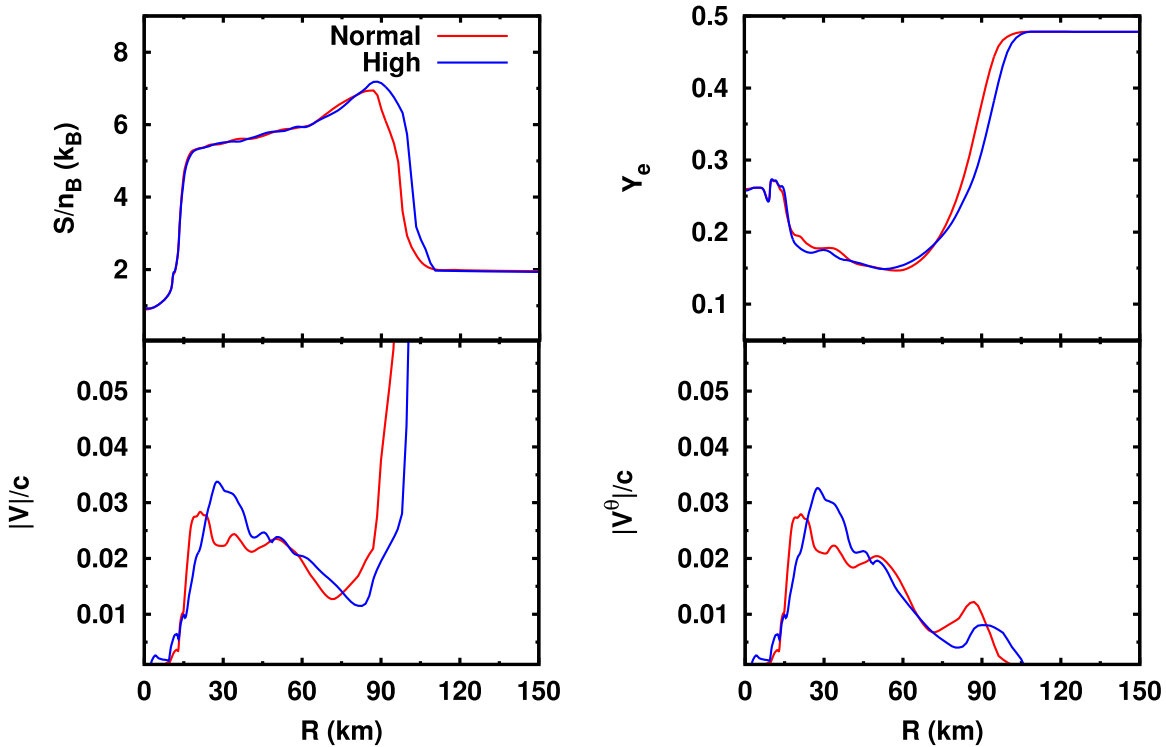
Figure 7. Angle-averaged radial profiles of fluid quantities. Upper left: entropy per baryon. Upper right: electron fraction. Bottom left: fluid speed. Bottom right: absolute values of lateral velocity. The red line shows the result of the normal-resolution simulation, while the blue lines correspond to the high-resolution simulation. The time is $t = 15$ ms postbounce.

clear-cut as in the previous paper, since the matter dynamics in this phase is chaotic, and small perturbations induced by the change in the angular resolution modify not only the neutrino distributions but also the matter configurations in the background substantially.

Richers et al. (2017) demonstrated that our Boltzmann solver tends to underestimate the forward peak in the angular distributions of neutrinos in momentum space at large radii if the number of angular mesh points is not large enough. This is actually just as expected and was indeed pointed out by Yamada et al. (1999) in their 1D study. As a matter of fact, neutrinos are moving almost radially at large distances from the neutrino sphere no matter what happens to them at small radii, and if the angular spread becomes smaller than the smallest width of the angular bin employed in the Boltzmann solver, it is no longer resolved.

Such properties of our Boltzmann solver should have some implications for the success or failure of explosion in our simulations, since the underestimation of the forward peak in the angular distribution in momentum space leads in turn to the overestimation of the local number density of neutrinos and, as a result, the overestimation of neutrino heating in the gain region. On the other hand, Richers et al. (2017) also found that the finite energy resolution tends to underestimate the neutrino heating. We then surmise from these results that the volume-integrated net energy deposition in the gain region is probably underestimated in the current simulations by a few percent.

For the study of the resolution dependence in the early postbounce phase, we conduct a high-resolution simulation for a short period as mentioned earlier. This time the matter distribution is not fixed but calculated just as in the ordinary run. We deploy $14(\bar{\theta}) \times 10(\bar{\phi})$ angular grid points over the entire solid angle while space and energy grids are unchanged

from the normal run. In Figure 7, we compare the radial profiles of some angle-averaged quantities at 15 ms after bounce between the models with the normal and high angular resolutions. As can be seen in this figure, the prompt shock wave is a bit faster and reaches a larger radius in the high-resolution model than in the normal-resolution model (upper left panel); in association with this, the deleptonization behind the shock is slightly stronger in the former around $20 \leqslant r \leqslant 40$ km (upper right). These are all attributed to the fact that the high-resolution simulation experiences a stronger prompt convection. This is indeed corroborated both in the fluid velocity and their lateral component in the convectively unstable region: they are a little larger in the high-resolution simulation consistently. As mentioned earlier, however, matter motions in this region are stochastic due to the chaotic nature of convection. The results would be different substantially if, for example, the initial time is changed even slightly. It is also difficult to isolate the influence of the angular resolution on the neutrino transport alone. More detailed resolution studies in dynamical settings will be reported elsewhere. With these caveats in mind, we will further compare some quantities of relevance in neutrino transport.

Figure 8 displays the radial profiles along two radial rays with $\theta = \pi/4$ (left column) and $\theta = 3\pi/4$ (right column) of some relevant quantities in the ν_e distribution at 15 ms after bounce. The neutrino energy is set to the average value at each point. In the top panels, the flux factors ($\bar{F}$) defined in Equation (7) are shown. One immediately recognizes that it is systematically smaller for the high-resolution case in the postshock region. This is not directly related to the angular resolution, though. Instead, it is simply because the shock radius is larger in the high-resolution run, and, as a result, the flux factor increases more slowly from the optically thick limit
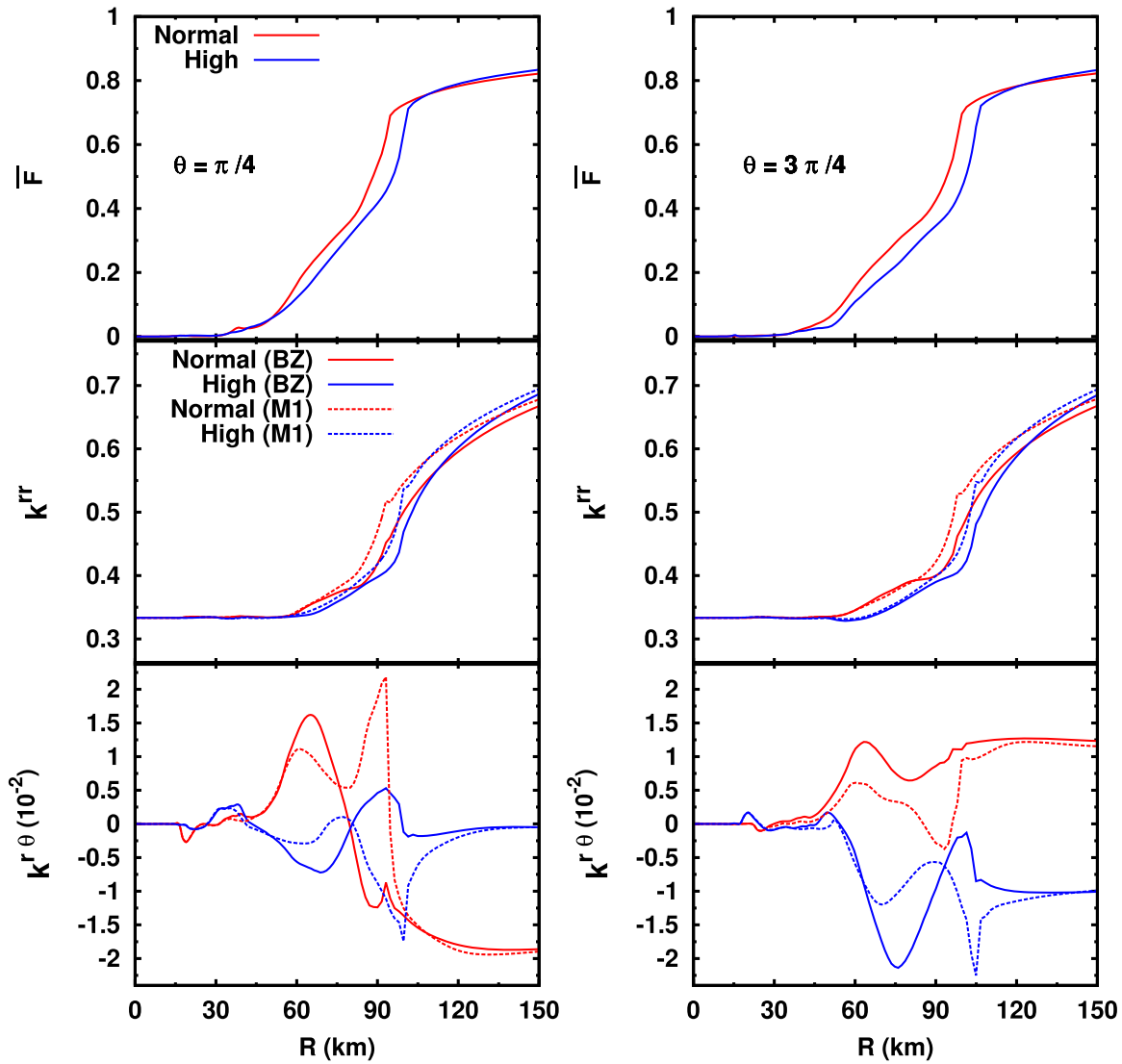
Figure 8. Flux factor (top) and the *rr* (middle) and *rθ* (bottom) components of the Eddington tensor for electron-type neutrinos. The left column presents the radial profiles along the radial ray with $\theta = \pi/4$, while the right one displays the same quantities but for $\theta = 3\pi/4$. The colors of lines and the time of the snapshot ($t = 15$ ms postbounce) are the same as in Figure 7.

($\bar{F} = 0$) to the thin limit ($\bar{F} = 1$). On the other hand, the flux factor is always smaller for the normal case than for the high-resolution case at large radii. This is a direct resolution effect; that is, the low-resolution simulation fails to reproduce the forward peak in the angular distribution at large radii.

The *rr* components of the Eddington tensor, k^{rr}, are shown in the middle panels of Figure 8. It is observed that they also increase a bit more slowly initially in the high-resolution run. This is again a mere consequence of the larger shock radius in that case. In these panels, we also display as additional dotted lines the same components of the Eddington tensor that are obtained with the M1 prescription. Except in the inner, optically thick region, they are always slightly greater than those obtained with the Boltzmann code for both resolutions. Considering the result in Richers et al. (2017) that low-resolution computations with the Boltzmann solver tend to underestimate k^{rr}, one may think that the results of the M1 prescription are closer to the true values. It should be noted, however, that the differences found here in k^{rr} between the Boltzmann and M1 results are larger than those obtained in Richers et al. (2017; see Figure 17 in their paper). This may

imply that the M1 prescription has its own problem in reproducing k^{rr} for the highly time-dependent and highly inhomogeneous matter distributions considered here. This issue will be further studied in our forthcoming paper. It is incidentally pointed out that the M1 prescription needs the flux factor to obtain the Eddington tensor (see Equations (5) and (6)). In the present comparison, it is provided by the Boltzmann solver, although it should be calculated on its own in the actual simulations with the M1 approximation. It is hence desirable to make comparisons by employing the results of such M1 simulations, which is another subject worth further investigations.

The bottom panels in Figure 8 are again the Eddington tensors but for the *rθ* component $k^{r\theta}$ this time. It should be noted first that $k^{r\theta}$ is very sensitive to the matter motion in the background. As a result, their profiles are quite different between the normal and high-resolution simulations, and it is rather difficult to discuss the convergence in the current dynamical setting. Nevertheless, it is evident that the Boltzmann and M1 results are substantially different from each other even qualitatively in the semitransparent region,
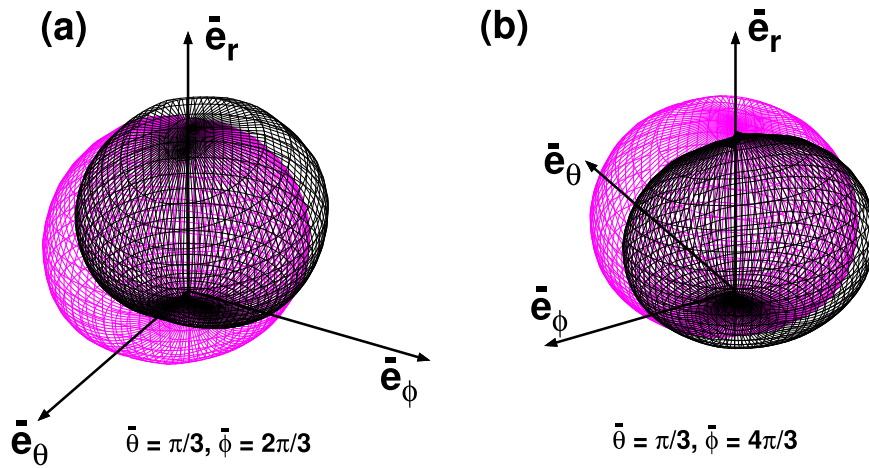
Figure 9. Same picture as in Figure 5 but for two different angular resolutions. The purple wired frame is identical to the same purple one in Figure 5. The black one is a high-resolution counterpart.

although they agree in both the optically thin and thick limits irrespective of resolutions. This is indeed consistent with the findings by Richers et al. (2017), who also came to the same conclusion that the difference in $k^{r\theta}$ between the Boltzmann transport with multiangles and the M1 prescription in the semitransparent regime is intrinsic and never reduced by increasing resolution. As will be demonstrated in Section 6, inaccurate $k^{r\theta}$ may give a $\sim$10% level of errors in the neutrino luminosity and, more importantly, will lead to qualitatively wrong lateral fluxes of neutrinos in the semitransparent region.

In Figure 9, we compare the angular distributions in momentum space obtained with the two resolutions. Note that the isotropic contributions are subtracted as previously in these pictures so that the anisotropies could be better recognized. In panel (a), the purple surface is identical to the one presented in Figure 5, while the black surface is the high-resolution counterpart. In Figure 9(b), we change the viewing angle to facilitate readers' understanding of the nonaxisymmetric features. As mentioned above, since the matter distributions in the background are different between the two cases, the neutrino angular distributions differ qualitatively. It is important, however, that the degree of asymmetry is even more prominent in the high-resolution simulation. This is again consistent with the finding in Richers et al. (2017) that $k^{r\theta}$ tends to be underestimated in low-angular-resolution simulations (see the right panel of Figure 15 in their paper).

6. Possible Implications of Off-diagonal Components on Supernova Dynamics

The existence of the nonaxisymmetric features in the angular distributions of neutrinos and the appearance of the nonvanishing off-diagonal components of the Eddington tensor as a result are the main novel findings in this paper. The legitimate question then is how significant they are for supernova dynamics. In order to fully address this issue, one must run additional simulations with some approximate neutrino transport scheme such as the ray-by-ray or M1 methods, which either completely ignore or employ a makeshift prescription for these nonaxisymmetric features, for the same progenitor, resolution, EOS, and input physics and make a detailed comparison, which is certainly beyond the scope of this paper. Instead, in this section, we compare different components of

the Eddington tensor quantitatively and discuss how the off-diagonal components might become important.

Note first that the equations for both the zeroth and first moments of the angular distribution include in principle all components of the Eddington tensor (see, e.g., Equations (3.37) and (3.38) in Shibata et al. 2011). It should be also pointed out that reaction rates of some neutrino–matter interactions such as nonisoenergetic scatterings and pair processes depend on higher-order moments including the Eddington tensor. Neglecting them may have some implications for CCSNe dynamics. Although this is an interesting issue and is in fact on our to-do list, in the following, we will limit our discussion to the advection part of the neutrino transport.

The principal part of the equations for the first angular moment or the flux can be approximately written as (see also Equation (3.38) in Shibata et al. 2011)

$$\partial_t(F^r) \sim -\partial_r(Ek^{rr}) - \frac{1}{r}\partial_\theta(Ek^{r\theta}), \tag{11}$$

$$\partial_t(F^\theta) \sim -\partial_r(Ek^{r\theta}) - \frac{1}{r}\partial_\theta(Ek^{\theta\theta}), \tag{12}$$

where we ignore collision terms and assume that the spacetime is flat and the background matter is axisymmetric and nonrotating. The off-diagonal component of Eddington tensor $k^{r\theta}$ appears in the second and first terms on the right-hand side of Equations (11) and (12), respectively. Note that it does not show up in the principal part of the zeroth-order equation for the energy density.

In Figure 10, we display radial profiles of the absolute values of the ratios of $\partial_\theta(Ek^{r\theta})/r$ to $\partial_r(Ek^{rr})$ (upper panels) and $\partial_r(Ek^{r\theta})$ to $\partial_\theta(Ek^{\theta\theta})/r$ (lower panels) on two radial rays with $\theta = \pi/4$ and $3\pi/4$ at 15 ms after bounce. In this analysis, we consider electron-type neutrinos alone, and their energy is set to the mean energy at each point. The results of both the normal- and high-resolution simulations are presented for comparison.

As seen in the upper panels, the radial flux is in general dictated mainly by k^{rr}, with $k^{r\theta}$ being at most 10%. This is certainly not a large value but still may not be ignored, since, as Burrows et al. (2018) claim, an accumulation of seemingly minor effects may turn out to be crucially important. On the other hand, $k^{r\theta}$ plays more important roles in the equation for
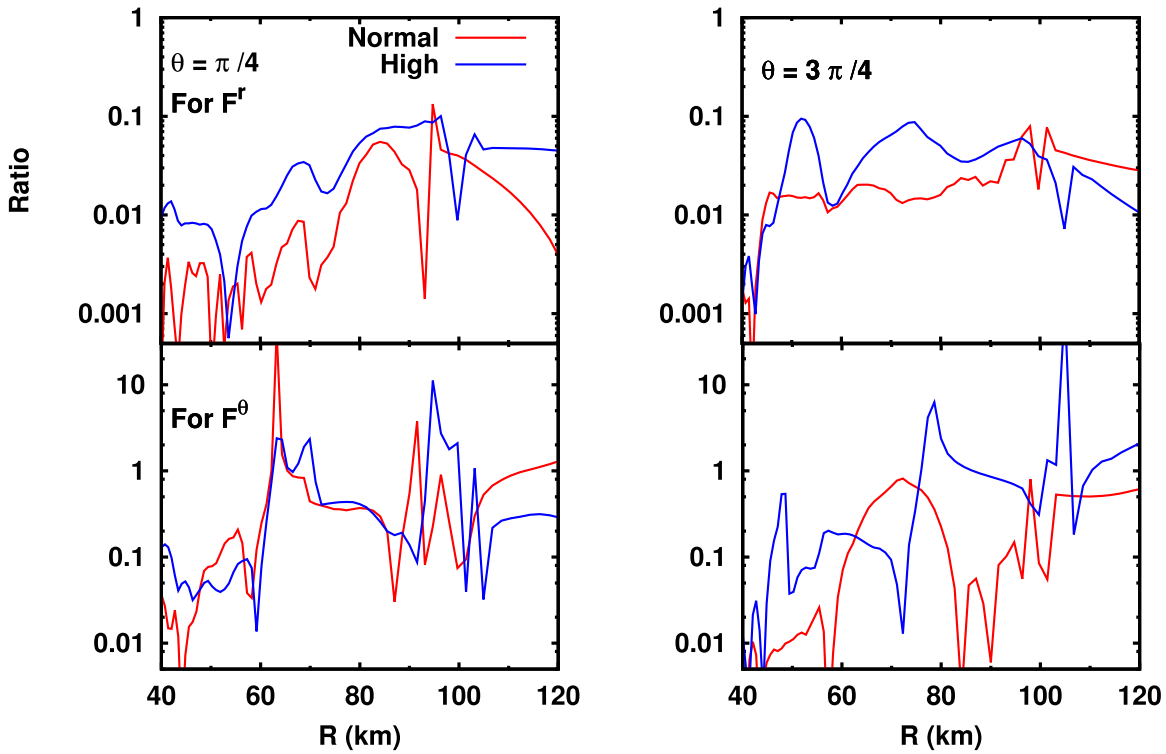
Figure 10. Radial profiles of the absolute ratios of $\partial_\theta (Ek^{r\theta})/r$ to $\partial_r(Ek^{rr})$ (upper panels) and $\partial_r(Ek^{r\theta})$ to $\partial_\theta(Ek^{\theta\theta})/r$ (lower panels). These quantities measure the relative importance of the terms on the right-hand side of Equations (11) and (12) for the r and θ components of neutrino flux. The left and right panels show profiles along the radial rays with $\theta = \pi/4$ and $3\pi/4$, respectively. Only electron-type neutrinos with the local mean energy are considered in this figure. The time is $t = 15$ ms postbounce.

the lateral component of neutrino flux, as demonstrated in the bottom panels. In fact, the ratio of the radial gradient of $Ek^{r\theta}$ to the lateral gradient of $Ek^{r\theta}/r$ exceeds unity in some postshock regions. This is also the case for the result of the high-resolution simulation, although the radial profiles themselves are quite different from those in the normal-resolution run, which is a consequence of the fact that matter distributions in the background become different between the two cases.

As discussed in Sections 4 and 5, the M1 prescription is not very successful in reproducing $k^{r\theta}$ in the semitransparent region, particularly in nonspherical settings. Although there is no artificially preferred direction in the M1 transport unlike in the ray-by-ray approximation, the lateral neutrino flux may still be inaccurate. It is misleading to argue that the Eddington tensor is reproduced again very well in the transparent regime with its off-diagonal component becoming negligible compared with the dominant k^{rr}. This is because the errors in the semitransparent region will not be confined there and will spread to the transparent region in time. The errors in the flux will lead to those in the Eddington tensor through the closure relation, which will again contribute to errors in the flux. This may eventually affect CCSNe dynamics. The quantitative assessment of this effect requires detailed comparisons in collaboration with other groups and is much beyond the scope of this first report of our new simulations.

We finally mention that the above analysis is based on the result of the early postbounce phase, in which the semitransparent region is highly dynamical owing to the prompt convection, and the $k^{r\theta}$ effect may be much smaller in the later phase. The errors in early times have some influence on the evolution in later times in principle, though. It should also be added that convections in the proto neutron star and other

hydrodynamic instabilities such as SASI and convections in the heating region occur more often than not even in the late phase. Again, quantitative assessments are certainly in order and will be studied in subsequent papers.

7. Comparison with Previous Works

In this section, we attempt to compare our results with other CCSNe simulations. The same progenitor model has been employed by many authors so far (Müller et al. 2012; Takiwaki et al. 2014; Summa et al. 2016). We note first that our results are qualitatively in line with them in that softer EOSs are advantageous for shock revival. It should be pointed out, however, that there are some studies in which softer EOSs including the LS EOS have smaller shock radii initially than the stiffer ones (see, e.g., Fischer et al. 2014), in apparent contradiction with our results.

According to Fischer et al. (2014), the difference in the shock trajectory originates mainly not from the stiffness of EOS but from the treatment of electron captures on heavy nuclei: representative heavy nuclei tend to be smaller in the softer LS EOS than in the stiffer STOS EOS, which is essentially the same as our FS EOS except for the single-nucleus approximation in the former, resulting in the greater deleptonization in the LS EOS during the collapse phase; this in turn leads to the smaller inner core and hence the weaker prompt shock wave for the LS EOS. Recall, however, that the electron capture rates employed in our simulation with the LS EOS are the same as those for the simulation with the FS EOS. As a result, the effects just mentioned are not taken into account in our current simulations, and the shock trajectories reflect the difference in the stiffness of EOSs alone.

The treatment of nuclear weak interactions consistent with the EOS employed is important to compute CCSNe dynamics accurately. We stress that the current approximate treatment is meant just for simplicity in models with EOSs that employ the single-nucleus approximation. We believe that multinucleus EOSs are indispensable for the quantitative study of the nuclear weak interactions mentioned above. Such a study is indeed under way (H. Nagakura et al. 2018, in preparation) with the multinucleus extension by Furusawa et al. (2017) of Togashi's EOS (Togashi & Takano 2013), which is based on the variational method for realistic nuclear potentials.

It is also important to point out that the shock expansion in our model looks less energetic than those in other simulations with the same progenitor model (see, e.g., Takiwaki et al. 2014). It is difficult to pin down the cause of the discrepancy, since there are many differences in input physics as well as numerical methods for hydrodynamics and neutrino transport, but the ray-by-ray approximation employed for neutrino transport in their simulations may be one of the main causes of the difference. In fact, Skinner et al. (2016) pointed out that the ray-by-ray approximation tends to artificially facilitate explosion in 2D, enhancing sloshing motions in axisymmetry. A similar concern was also expressed by Sumiyoshi et al. (2015), who showed that the asymmetry in the neutrino heating tends to be overestimated in the ray-by-ray approximation. More detailed comparisons in collaborations with other groups are required to substantiate the claim, though.

8. Summary and Discussion

We have presented the first report of spatially axisymmetric CCSNe simulations with the full Boltzmann neutrino transport. We have found both similarities and differences between the two models with two different nuclear EOSs. On the one hand, the neutrino luminosities and mean energies as well as the postshock morphologies except the scale are very similar between the two. This seems to be a consequence of the cancellation of the stronger bounce that would be expected in the softer LS EOS by the greater electron captures that produced the smaller inner core in the LS EOS model. On the other hand, the neutrino-heating efficiency and the mass in the gain region are consistently higher for the LS EOS. This seems to be due to more vigorous turbulent motions in the postshock flow for the LS EOS than for the FS EOS, a fact that results in the greater expansion of the shock wave: it has reached $\sim$700 km by 300 ms after bounce, and its maximum radius is still growing.

By virtue of the multiangle treatment in our simulations, we have found interesting features in the neutrino distribution in momentum space, such as the lack of axisymmetry with respect to the local radial direction and the nonvanishing off-diagonal component of the Eddington tensor. With the aid of our previous analyses in Richers et al. (2017) and an additional high-resolution simulation for the early postbounce phase, we have estimated that the current simulations may have underestimated the neutrino-heating rate by a few percent owing to rather low angular and energy resolutions in momentum space. The possible effects of the off-diagonal component of the Eddington tensor, $k^{r\theta}$, on neutrino transport have also been discussed quantitatively: it plays a nonnegligible role in the time evolution of neutrino fluxes; it may give a $\sim$10% level of contribution to the neutrino luminosity; and, more importantly,

it can be a dominant factor in the time evolution of lateral flux in the semitransparent region.

We have found an interesting correlation/anticorrelation in $k^{r\theta}$ between ν_e and $\bar{\nu}_e$ depending on the radius. It is related to the lateral fluxes of these neutrinos. It will be interesting to see how well the M1 approximation fares in reproducing these features and hence the lateral fluxes. The close comparison between our Boltzmann solver and other approximate methods possibly in collaboration with other groups will be indispensable in assessing critically and quantitatively the significance of the findings in this paper for the CCSNe dynamics. It will also enable us to calibrate and possibly improve the prescriptions, which should be given by hand in approximate transport schemes. This is indeed important practically, since our method is very costly in terms of required numerical resources.

We have made an attempt to compare our results with those obtained by other groups for the same progenitor model. We have found that the general trend that softer EOSs are favorable for shock revival is also true of our simulations. On the other hand, the continuous shock expansion observed for the softer LS EOS looks less energetic than that found by others. Although this seems to be consistent with the finding by Skinner et al. (2016) that the ray-by-ray approximation in spatial axisymmetry may artificially enhance shock revival, more detailed comparisons are certainly necessary to draw some conclusions.

There are also certainly many other issues remaining to be addressed. The top priority is to make detailed comparisons with other approximate methods to assess the importance of multiangle treatments for supernova dynamics by possibly collaborating with other groups. We will also explore other progenitors with different masses. The EOS dependence should be further clarified. Rotation is another concern, since the angular distribution in momentum space is then qualitatively changed: for example, the principal axis will not be aligned with the radial direction in general, and another off-diagonal component, $k^{r\phi}$, will no longer be vanishing. We are currently implementing general relativity in our code to investigate its influences, which are expected to be nonnegligible. The angular distributions for different species of neutrinos we obtained in this study are valuable in their own right, for example, the analysis of collective oscillations of neutrino flavors (Duan et al. 2010; Mirizzi 2013; Capozzi et al. 2017; Izaguirre et al. 2017), which feed on the differences in the angular distributions among different neutrino species. They are currently being investigated, and the results will be reported elsewhere.

ORCID iDs

Wakana Iwakami ⓘ https://orcid.org/0000-0003-4959-069X
Kohsuke Sumiyoshi ⓘ https://orcid.org/0000-0002-9224-9449
Shoichi Yamada ⓘ https://orcid.org/0000-0002-2166-5605

References

Andresen, H., Müller, B., Müller, E., & Janka, H.-T. 2017, MNRAS, 468, 2032
Bionta, R. M., Blewitt, G., Bratton, C. B., Casper, D., & Ciocio, A. 1987, PhRvL, 58, 1494
Bruenn, S. W. 1985, ApJS, 58, 771
Bruenn, S. W., Lentz, E. J., Hix, W. R., et al. 2016, ApJ, 818, 123
Bruenn, S. W., Mezzacappa, A., Hix, W. R., et al. 2013, ApJL, 767, L6
Buras, R., Rampp, M., Janka, H.-T., & Kifonidis, K. 2006, A&A, 447, 1049
Burrows, A., Vartanyan, D., Dolence, J. C., Skinner, M. A., & Radice, D. 2018, SSRv, 214, 33
Capozzi, F., Dasgupta, B., Lisi, E., Marrone, A., & Mirizzi, A. 2017, PhRvD, 96, 043016
Cappellaro, E., Turatto, M., Benetti, S., et al. 1993, A&A, 273, 383
Diehl, R., Halloin, H., Kretschmer, K., et al. 2006, Natur, 439, 45
Dolence, J. C., Burrows, A., & Zhang, W. 2015, ApJ, 800, 10
Duan, H., Fuller, G. M., & Qian, Y.-Z. 2010, ARNPS, 60, 569
Fischer, T., Hempel, M., Sagert, I., Suwa, Y., & Schaffner-Bielich, J. 2014, EPJA, 50, 46
Foglizzo, T., Scheck, L., & Janka, H.-T. 2006, ApJ, 652, 1436
Furusawa, S., Nagakura, H., Sumiyoshi, K., Kato, C., & Yamada, S. 2017, PhRvC, 95, 025809
Furusawa, S., Sumiyoshi, K., Yamada, S., & Suzuki, H. 2013, ApJ, 772, 95
Furusawa, S., Yamada, S., Sumiyoshi, K., & Suzuki, H. 2011, ApJ, 738, 178
Hirata, K., Kajita, T., Koshiba, M., Nakahata, M., & Oyama, Y. 1987, PhRvL, 58, 1490
Iwakami, W., Nagakura, H., & Yamada, S. 2014, ApJ, 786, 118
Izaguirre, I., Raffelt, G., & Tamborra, I. 2017, PhRvL, 118, 021101
Juodagalvis, A., Langanke, K., Hix, W. R., Martínez-Pinedo, G., & Sampaio, J. M. 2010, NuPhA, 848, 454
Just, O., Obergaulinger, M., & Janka, H.-T. 2015, MNRAS, 453, 3386
Kuroda, T., Takiwaki, T., & Kotake, K. 2016, ApJS, 222, 20
Langanke, K., & Martínez-Pinedo, G. 2000, NuPhA, 673, 481
Langanke, K., Martínez-Pinedo, G., Sampaio, J. M., et al. 2003, PhRvL, 90, 241102
Lattimer, J. M., & Douglas Swesty, F. 1991, NuPhA, 535, 331
Lentz, E. J., Bruenn, S. W., Hix, W. R., et al. 2015, ApJL, 807, L31
Lentz, E. J., Mezzacappa, A., Messer, O. E. B., et al. 2012, ApJ, 747, 73
Li, W., Leaman, J., Chornock, R., et al. 2011, MNRAS, 412, 1441
Maoz, D., & Badenes, C. 2010, MNRAS, 407, 1314
Marek, A., & Janka, H.-T. 2009, ApJ, 694, 664
Melson, T., Janka, H.-T., & Marek, A. 2015, ApJL, 801, L24
Mirizzi, A. 2013, PhRvD, 88, 073004
Müller, B., Janka, H.-T., & Marek, A. 2012, ApJ, 756, 84
Müller, B., Melson, T., Heger, A., & Janka, H.-T. 2017, MNRAS, 472, 491
Nagakura, H., Iwakami, W., Furusawa, S., et al. 2017, ApJS, 229, 42
Nagakura, H., Sumiyoshi, K., & Yamada, S. 2014, ApJS, 214, 16
O'Connor, E., & Couch, S. 2015, arXiv:1511.07443
Ott, C. D., Burrows, A., Dessart, L., & Livne, E. 2008, ApJ, 685, 1069
Pan, K.-C., Liebendörfer, M., Hempel, M., & Thielemann, F.-K. 2016, ApJ, 817, 72
Reed, B. C. 2005, AJ, 130, 1652
Richers, S., Kasen, D., O'Connor, E., Fernández, R., & Ott, C. D. 2015, ApJ, 813, 38
Richers, S., Nagakura, H., Ott, C. D., et al. 2017, ApJ, 847, 133
Roberts, L. F., Ott, C. D., Haas, R., et al. 2016, ApJ, 831, 98
Shibata, M., Kiuchi, K., Sekiguchi, Y., & Suwa, Y. 2011, PThPh, 125, 1255
Skinner, M. A., Burrows, A., & Dolence, J. C. 2016, ApJ, 831, 81
Sumiyoshi, K., Suzuki, H., Yamada, S., & Toki, H. 2004, NuPhA, 730, 227
Sumiyoshi, K., Takiwaki, T., Matsufuru, H., & Yamada, S. 2015, ApJS, 216, 5
Sumiyoshi, K., & Yamada, S. 2012, ApJS, 199, 17
Summa, A., Hanke, F., Janka, H.-T., et al. 2016, ApJ, 825, 6
Takiwaki, T., Kotake, K., & Suwa, Y. 2014, ApJ, 786, 83
Tammann, G. A., Loeffler, W., & Schroeder, A. 1994, ApJS, 92, 487
Togashi, H., & Takano, M. 2013, NuPhA, 902, 53
van den Bergh, S., & Tammann, G. A. 1991, ARA&A, 29, 363
Woosley, S. E., Heger, A., & Weaver, T. A. 2002, RvMP, 74, 1015
Yamada, S., Janka, H.-T., & Suzuki, H. 1999, A&A, 344, 533